Towards superconducting spintronics with RuO2 and CrO2 nanowires

Prateek, K.

3

Growth and Properties of CrO_2 Nanowires

Chromium dioxide (CrO_2) nanowires with their half-metallic ferromagnetic properties have shown great promise in spintronics applications. However, growth of such wires remains challenging. We used the Selective Area growth method to fabricate high quality epitaxial CrO_2 wires on a TiO_2 substrate, using trenches oriented both along the substrate [001] c-axis and along the [010] b-axis, which are the magnetically easy and hard axis of the wire, respectively. We investigated the morphology of the wires by high-resolution transmission electron microscopy (TEM) and measured their physical properties, in particular magnetoresistance (MR) and the Anomalous Hall Effect (AHE). TEM images showed that the morphology of the wires grown along the two axes are very different. MR data show very sharp switching for c-axis grown wires (the easy axis), even for quite large wire widths. The AHE is found to be different for c-axis wires and b-axis wires, which we argue to be due to a different wire morphology on the nanoscale.

This chapter is based on the paper published in *Journal of Physics and Chemistry of Solids* **178**, 111350 (2023).

3.1. Introduction

Binary oxides with the rutile structure are currently of interest again, especially the ones which show good metallic conductivity. In the area of spintronics, in particular CrO_2, RuO_2 and IrO_2, plus substituted alloys have been studied in recent years. CrO_2 is a half-metallic ferromagnet (HMF) [1], and therefore fully spin-polarized; RuO_2 was recently found to be a weak collinear antiferromagnet [2] and is a prime candidate for showing the Crystal Hall effect [3]; and IrO_2 has been studied for its use as spin current detector [4]. The HMF nature of CrO_2 makes it particularly interesting for spintronics applications, with recent studies reporting on the expected performance in magnetic tunnel junctions[5], on the resistance of single domain walls[6], on Gilbert damping in epitaxial films[7], and on spin-curvature induced resistivity[8]. A significant drawback is that the compound is metastable at ambient conditions [9]. Single crystals can be synthesized using high pressure, but thin films cannot be grown with the standard physical deposition methods such as molecular beam epitaxy, sputtering, or pulsed laser deposition. Instead, a chemical vapor deposition (CVD) method has to be used, in which a precursor gas, mixed with oxygen, is led over a heated substrate. At the right substrate temperature, dissociation takes place, and CrO_2 is formed [10, 11].

Because of relatively good lattice matching, the substrate of choice for the deposition is TiO_2, and, to a lesser degree, Al_2O_3. Magnetotransport properties of thin films grown by the CVD method grown on either substrate have been extensively investigated [12–15]. One salient finding for films grown on TiO_2 is that the easy and hard axes for the magnetization lie along different directions in the crystal (easy axis is the [001] *c*-axis) than in thin and inevitably slightly strained films (easy axis often is the [010] *b*-axis). It was even observed that, through strain release, this can lead to a change of the easy (hard) axis direction, both as function of temperature and film thickness [13, 16]. Observations of biaxial anisotropy can also be explained through this relaxation mechanism [16–18].

Much of this work has been done on films, but for incorporating CrO_2 in mesoscopic structures, the grainy nature of the films is a serious impediment. Substrate treatment plays a role in the grain morphology [16, 19], and influence of grain boundaries was observed in the form of Intergrain Tunneling Magnetoresistance (ITMR) [14, 15]. Grain boundaries can be avoided, however, by using the technique of Selective Area (SA) growth, which allow to grow high-quality nanowires and other structures. The technique is based on the fact that, at the required deposition conditions, CrO_2 grows epitaxially on TiO_2, but does not form any deposit on silicon oxide (SiO_x) [20]. By etching a trench in a SiO_x layer deposited on the TiO_2 substrate, high quality nanowires can be grown. The magnetotransport properties of such wires

were studied [21–24] and more recently, they were used to investigate spin-triplet superconductivity [25] and the resistance of a single domain wall (DW)[26], which is of particular interest in half metals.

Given the fact that CrO_2 nanowires are of clear interest for a variety of spintronics phenomena as referred to above, little attention has been paid to the growth and the morphology. It was reported that lateral overgrowth occurs when the growing layer reaches the top of the SiO_x mask, and is accompanied by the formation of side facets [20, 25]. but also that the initial growth can be quite defective, with a high dislocation density [20], or even voids [25].
In this thesis, we make a detailed study of the morphology of SA-grown nanowires, and combine this with magnetotransport experiments. We focus on growing wires on TiO_2(100), with directions along the substrate *c*-axis and *b*-axis (the magnetic easy and hard axis, respectively) for trench and wire widths in the range of 0.5 μm to 2 μm. We use atomic force microscopy (AFM), but more importantly Transmission Electron Microscopy (TEM) to study the morphology. The main and new finding of the study is that the wires along the two axes differ in important details, both with respect to the morphology and with respect to the magnetotransport. Most surprising, possibly, is that the Anomalous Hall Effect (AHE) is different for the two types of wires. This is very different from what is found when bars are etched in films by Ar-ion etching along the magnetic easy and hard directions [14, 15], which can be understood from the difference in fabrication.

The chapter is structured as follows. First we give a detailed description of the nanofabrication process which leads to SA-grown nanowires. Then we concentrate on wire widths around 0.5 μm and give TEM and electrical and magneto-transport results for the *c*-axis (magnetic easy axis) wires, followed by the results for the *b*-axis (magnetic hard axis) wires. Because of in particular the AHE results, we finally present data on larger hard-axis wire widths, up to 2 μm.

3.2. Selective area growth of CrO_2 nanowires

CrO_2 and TiO_2 both crystallize in the rutile structure, with a tetragonal unit cell. Both structures are shown in the Appendix, sec.3.8.2. We use (100) oriented TiO_2 substrates, which means that the *b*- and *c*-axes of the structure lie in the film plane. For CrO_2, the lattice parameters are $a = b = 0.4421$ nm and $c = 0.2916$ nm. For TiO_2 the values are $a = b = 0.4594$ nm, $c = 0.2958$ nm. The CrO_2 values in the plane are therefore smaller by -3.8% (*b*-axis) and -1.5% (*c*-axis), resulting in tensile strain. In CrO_2 films on HF-treated substrates, comparatively lower strain along *c*-axis leads to crystallites oriented along the *c*-direction [16]. As was already mentioned, the

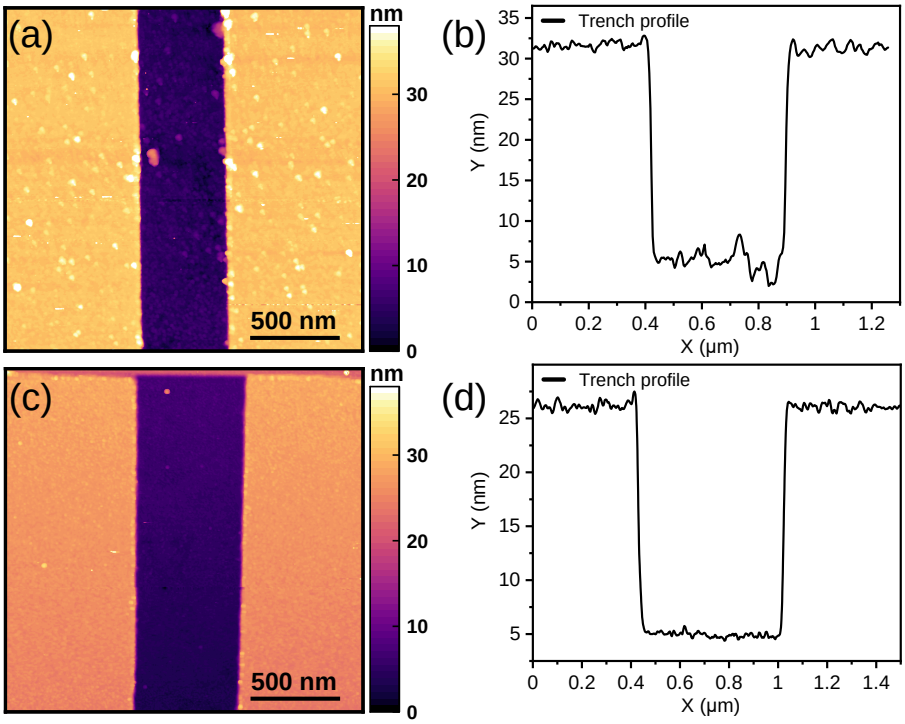

Figure 3.1: AFM images of etched SiO_x masks on top of TiO_2 substrates. The thickness of the SiO_x layer in this case is 19 nm. (a) Surface scan of a section of a mask with the trench, taken from an overetched trench (depth 26 nm). (b) The corresponding line profile of the trench showing a rough and damaged TiO_2 surface at the bottom. (c) Surface scan of an optimally etched trench (depth 21 nm). (d) The corresponding line profile showing a smooth surface at the bottom.

crystallographic *c*-axis is the magnetic easy axis, while the *b*-axis is the hard axis. Hereafter, we call *c*-axis oriented wires as 'easy' wires and *b*-axis oriented wires as 'hard' wires.

Making the SiO_x mask starts with a HF etch of the TiO_2 substrate, depositing a SiO_x layer with a typical thickness of about 20-25 nm, and electron beam patterning to create a positive resist mask with the desired device structure. The trench is selectively etched into the SiO_x by reactive ion etching. After that, CrO_2 nanowires are grown in the trenches using CVD in a two-zone furnace, where the substrate temperature is kept at 390°C, while the precursor CrO_3 is heated to 260°C in the presence of a flow of O_2 carrier gas. The temperature window for growth is very narrow, not more than 10°C. We found that, for successful growth, it is critical to neither underetch nor overetch the trench. The result of underetching is clear, the trench bottom will then still be formed by SiO_x, and CrO_2 cannot grow. Overetching

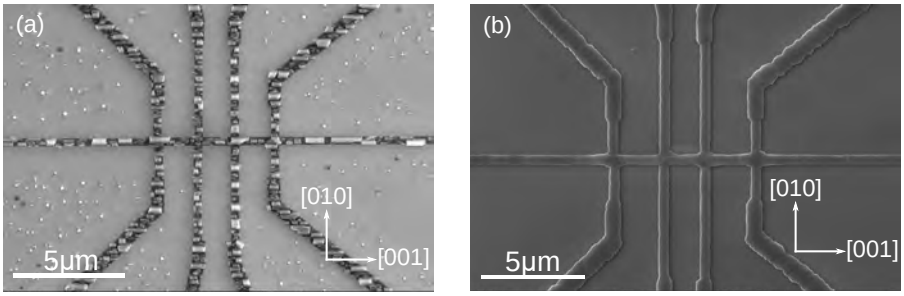

Figure 3.2: SEM images comparing (a) growth in an overetched and rough trench bottom and (b) the growth in a smooth trench. The horizontal direction [001] in the images is the crystal c-axis, which is also the orientation of the long axis of the crystallites in (a).

is also detrimental, however, as it damages the underlying TiO_2 surface. Fig. 3.1 compares the AFM images of two trenches, an overetched one with a depth of about 26 nm, and an optimally etched one of 21 nm. Fig. 3.1(a) has a rough bottom while Fig. 3.1(c) is very smooth, and that translates into the growth. Fig. 3.2(a) shows SEM images of wire growth on a rough trench surface. This causes formation of unevenly distributed CrO_2 crystallites that fail to merge timely, resulting in a broken wire growth. However, for an optimally etched smooth trench as seen in Fig. 3.2(b), the crystallites merge completely at the bottom surface of the trench and we get high quality epitaxial growth. The depth window where we get desired trench quality to facilitate good nanowire growth is rather small, not more than a few nm. That means not only the etching, but also the SiO_x deposition has to be monitored carefully, while also the uniformity of the deposition is important. In our optimized procedure we deposit on both a 'device' substrate and a 'test' substrate in the same run. On the test substrate we measure the actual SiO_x thickness by small-angle X-ray diffraction, an etch run is performed, and AFM is used to measure the resulting trench depth. From AFM images the etch rate is computed and used in growing the wire on the 'device' substrate. Afterwards, devices are inspected by SEM. We grew CrO_2 nanowires along different angles with respect to the TiO_2 substrate axes. Here, we will focus on the easy [001] and hard [010] wires while intermediate angles are discussed in the Appendix, sec. 3.8.4[27].

As a side note, CrO_2 nanowires have also been SA-grown in considerably deeper trenches, of about 100 nm [24, 26]. We have not investigated growth in such deeper trenches.

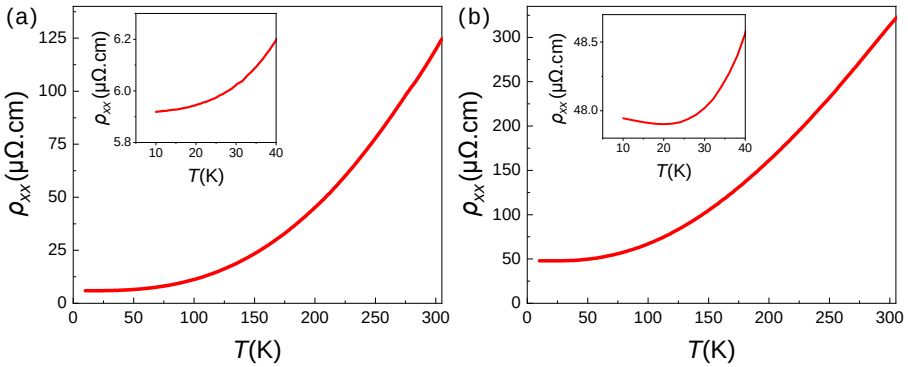

Figure 3.3: Resistivity as a function of temperature for (a) an easy wire (width 580 nm, thickness 105 nm, contact distance 4 μm); the inset shows the positive temperature coefficient of resistance at lower temperature. (b) a hard wire (width 610 nm, thickness 60 nm, contact distance 2.5 μm); the inset shows an upturn in resistance below 20 K.

3.3. Resistivity as function of temperature: easy and hard wires

The temperature dependence of the resistivity, ρ(T), is an important characterization parameter. The transport measurements were carried out over a temperature range from 300 K to 10 K in a Physical Property Measurement System (PPMS). Fig. 3.3(a) shows ρ(T) for a typical easy wire: a width around 580 nm, a thickness of 105 nm and with a distance between the contacts around 4 μm. The room temperature resistivity ρ_{300} is 120 μΩcm while the low-temperature (10 K) value ρ_0 is 5.9 μΩcm. This gives a residual-resistance ratio (RRR, the ratio between ρ_{300} and ρ_0) of ≈ 21. The wire has a positive temperature coefficient of resistance at all temperatures, also at the lowest temperatures, as seen in the inset of Fig. 3.3(a). This suggests very little or no grain boundary scattering of electrons [24]. We also notice that in our easy wire, while ρ_0 is similar, ρ_{300} is more than 2 times lower compared to previous studies on films and SA-grown nanowires [12, 15, 24], indicating higher conductivity (or better metallic behavior) of our nanowires at room temperature. This suggests better crystal quality of the wires, which is supported by TEM analysis on an easy wire that is discussed in the next section.

As mentioned in section 3.2, we observe that for both easy and hard wires, the preferred direction of crystallite growth is the c-axis, i.e. along the easy wire length, but along the hard wire width. This makes growing hard wires more difficult. They are more sensitive to the trench depth, and also the width cannot be too small. We found the minimal width for reproducible good growth to be about 500 nm, unlike easy wires which we could grow down to a width of ≈ 100 nm.

Fig. 3.3(b) shows ρ(T) for a similar but hard wire: a width around 610 nm, a thickness of 60 nm, and distance between the contacts of 2.5 µm. For this wire, ρ_{300} is 314 µΩcm while ρ_0 is 47 µΩcm, yielding an RRR of 6.7. These numbers are similar to the epitaxial hard wires measured in Ref. [24] but significantly higher than Ar ion-etched wires from thin films [15]. Since the growth kinetics for a SA-grown hard wire is totally different from the hard wire obtained from a CrO_2 film through Ar ion-etching, it is not reasonable to compare the ρ(T) measurements. We further observe that there is a small upturn in ρ at low temperature around 20 K, as seen in inset of Fig. 3.3(b). This indicates the presence of grain boundaries in the nanowire, that become more dominant at lower temperatures [24]. The morphology of the hard wire is further explained in details in section 3.5.1.

3.4. Easy axis wires

3.4.1. TEM analysis

Using high-resolution transmission electron microscopy (HR-TEM), we analyzed the crystal structure and orientation of the nanowires and compared them to the single crystal TiO_2 substrate. A low magnification image of a cross-section of the easy nanowire is given in Fig. 3.4(a) wherein, we can see the TiO_2 substrate at the bottom with the CrO_2 nanowire on top of TiO_2. The nanowire grew inside the 517 nm wide trench that was etched in the SiO_x mask (shown in white in Fig. 3.4(a)) that was deposited on the TiO_2 substrate. The cross-section also clearly shows no CrO_2 growth on top of the SiO_x mask. Contrary to previous report by Singh et. al,[25] we observe no overgrowth for the easy wire. However, we still observe the formation of side facets. These facets are oriented at a 90° angle with respect to the edge of the SiO_x mask and a 45° angle with respect to the TiO_2 substrate, as seen near the bottom right in Fig. 3.4(a). The nanowire is 75 nm high and 525 nm wide at its highest and widest point, respectively. The trapezoidal shape of the wire is only interrupted by a triangular divot. A higher resolution image of the area underneath the divot is shown in the Appendix, Fig. 3.10(a). The area underneath the divot, right at the interface between the TiO_2 substrate and the CrO_2 nanowire, has several regions with a darker contrast. An HR-TEM image of one of these regions, highlighted by the white box in Fig. 3.4(a), is shown in Fig. 3.4(b). This atomic resolution image shows the TiO_2 substrate in the bottom left corner and two different crystal CrO_2 domains on the right. The fast Fourier transform (FFT) of the area in the blue box helps us to establish that the TiO_2 crystal substrate is oriented along the [001] zone-axis as expected for the easy nanowire. As mentioned before in section 3.2, we would expect the CrO_2 nanowire to grow epitaxially because of the minor lattice mismatch between the TiO_2 and the CrO_2. However, we observe two different CrO_2

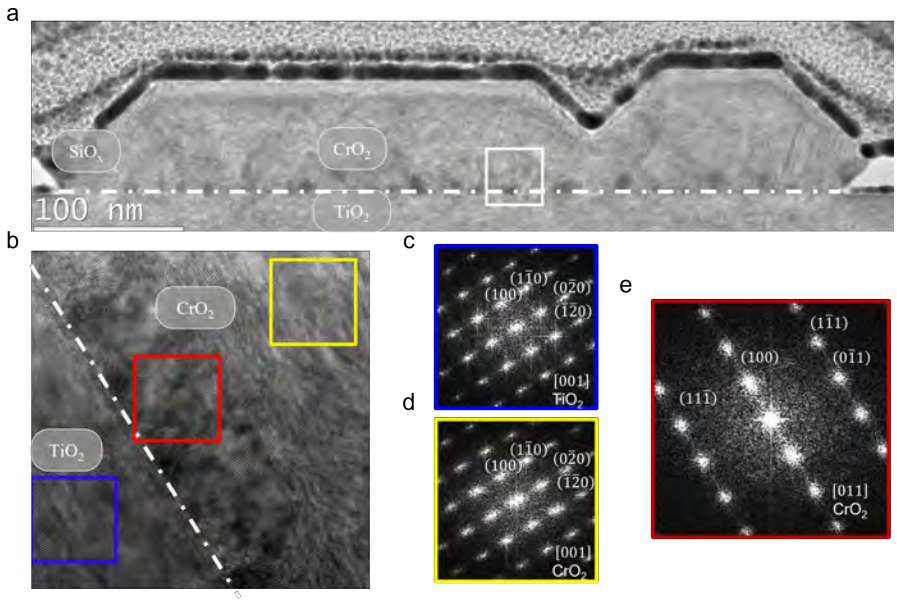

Figure 3.4: TEM inspection of a cross-section from the CrO_2 nanowire along the easy axis. (a) Low resolution TEM image of the TiO_2 substrate at the bottom and the partially grown CrO_2 nanowire in between the SiO_x mask. (b) High-resolution TEM image of the dark cluster highlighted in (a) showing the TiO_2 substrate at the bottom (blue box) and two CrO_2 crystal domains with different crystal orientations (red and yellow boxes). (c-e) The indexed fast Fourier transforms of the areas highlighted in (b) (blue box in (c), yellow box in (d), red box in (e)). The FFT's show that most of the nanowire grows epitaxially with the substrate, but some crystal domains have a different orientation than the substrate.

crystal orientations in Fig. 3.4(c). Indeed, the FFT of the area inside the yellow box, just like the bulk of the nanowire, corresponds to the diffraction pattern of CrO_2 orientated along the [001] zone axis. However, the FFT of the area in the red box corresponds to the diffraction pattern of CrO_2 oriented along the [011] zone axis. This shows that the bulk of the CrO_2 grows epitaxially on the TiO_2 substrate, but some small regions have a different crystal orientation than the TiO_2 substrate. An atomic model of the different crystal domains is displayed in Fig. 3.10(b) of the Appendix. These irregularities in the crystal orientation can mostly be found at the interface between the TiO_2 substrate and the CrO_2 nanowire or at the interface with the SiO_x mask. This is probably due to imperfections in the TiO_2 substrate caused by the over-etching of the SiO_x mask or conversely by leaving a SiO_x residue by under-etching the SiO_x mask.

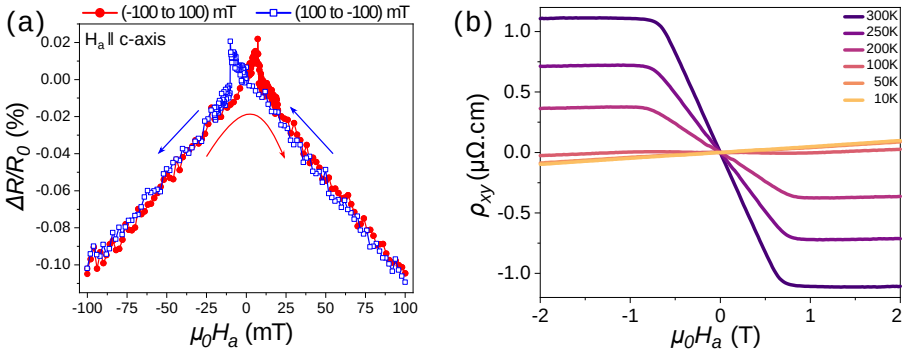

Figure 3.5: Magnetotransport measurements on the same 580 nm wide easy wire as shown in Fig. 3.3. (a) In-plane longitudinal MR measured at 10K. The external magnetic field H_a is parallel to the easy wire i.e. (H_a || c-axis [001]). The field is swept from −100 mT to 100 mT (filled red circles) and then from 100 mT to −100 mT (open blue squares). The arrows in blue and red show the sweep direction for the respective curves. (b) Hall resistivity as a function of external out-of-plane field for the same easy wire measured at various temperatures between 10 K to 300 K. A current of 100 μA is applied in both cases.

3.4.2. Magnetotransport

We further characterized CrO_2 wires through magnetotransport measurements for different magnetic field orientations and at different temperatures. Fig. 3.5(a) shows the longitudinal magnetoresistance (MR) behavior $(R(H_a) - R(0))/R(0) = \Delta(R)/R(0)$ at 10 K, where H_a is the magnetic field along the wire axis, for the same 580 nm wide easy wire as measured in section 3.3. We find that the MR behavior differs from that of previous SA-grown wires of comparable or smaller width. In contrast to earlier studies that showed parabolic behavior and an extended switching range for a similar wire width, we find that the magnetization switching is sharp, with only very little supralinear behavior when approaching the coercive field H_c at around 10 mT [24]. In earlier research, even 100 nm-wide wires did not exhibit the same degree of sharp switching as this 580 nm-wide wire demonstrates. We view this as further evidence of the high crystalline quality of the wires, possibly as a consequence of using quite shallow trenches with very well controlled bottom surfaces.

Fig. 3.5(b) shows measurements of the Hall resistivity as a function of external out-of-plane (OP) field for different temperatures in a range from 300 K to 10 K. The data are represented as ρ_{xy} as function of magnetic field, with $\rho_{xy} = V_{xy}d/I$, where V_{xy} is the transverse voltage, I is the measurement current, and d is the thickness of the wire. The behavior can, as expected, be described by

$$\rho_{xy}(H_a) = \mu_0 (R_0 H_a + R_{AHE} M) \tag{3.1}$$

with R_0 the normal Hall coefficient, R_{AHE} the anomalous Hall coefficient, and M the magnetization of the ferromagnet. We see that R_{AHE} decreases from 300 K in a roughly linear fashion down to 100 K, where zero is reached. Below 100 K, R_{AHE} is zero. This behavior is well known, and attributed to a Berry phase, caused by an increasing amount of spin defects with increasing temperature that produce a non-trivial spin background through which the carriers move [28, 29].

The values of R_{AHE} can be compared to earlier work. According to Eq. 3.1, $R_{AHE} = \rho_{xy}(0)/(\mu_0 M)$, but the use of different units and the ambiguity with respect to the value of M (the saturation value at 300 K is lower than at 10 K, and lower than inferred from the saturation moment of 2 μ_B/Cr-atom) make it more straightforward to compare values for $\rho_{xy}(0)$ at 300 K. From Fig. 3.5(b) we find $\rho_{xy}(0)$ = 1.1 μΩcm for the 580 nm wide easy wire. For films measured by the van der Pauw method, values of 1.4 μΩcm[11] and 0.8 μΩcm [30] are reported. For etched films with a bar along the easy axis, two studies report 1.5 μΩcm[29, 31]. No values have been reported for SA-grown wires. Interestingly, the three films yielding similar values were grown on a TiO_2 substrate, while the film with a significantly lower value was grown on Al_2O_3. It is well known that such films have a different morphology, because of the hexagonal mesh of that substrate [31, 32].

3.5. Hard axis wires

3.5.1. TEM analysis

We also investigated the crystal structure of the hard nanowire. The cross-section of such a wire can be seen in Fig. 3.6(a). Here we can see the TiO_2 substrate at the bottom with the CrO_2 nanowire in between the SiO_x mask. Like for the easy axis nanowire, the CrO_2 grew inside the 516 nm wide trench that was etched in the SiO_x mask. The nanowire is 522 nm wide and 99 nm high at its widest and highest point, respectively. Similar to the easy wire, we observe faceted edges. Although these are less well defined than the faceted edges of the easy wire, we can still determine that the facets make roughly a 45° angle with the TiO_2 substrate. Furthermore, the CrO_2 only grows on top of the TiO_2 substrate, which means that there is again no overgrowth over the SiO_x mask. An HR-TEM image of the interface between the TiO_2 substrate and the CrO_2 nanowire is shown in Fig. 3.6(b). The FFT of the region enclosed in the blue box is shown in Fig. 3.6(c). As expected, this pattern corresponds to the diffraction pattern of TiO_2 oriented along the [0 1 0] zone axis. The FFT of the area of CrO_2 inside the red box is depicted in Fig. 3.6(d). Here, we can see the same basic diffraction pattern corresponding to CrO_2 oriented along the [0 1 0] zone axis, but more diffraction spots are visible. These Moiré patterns belong

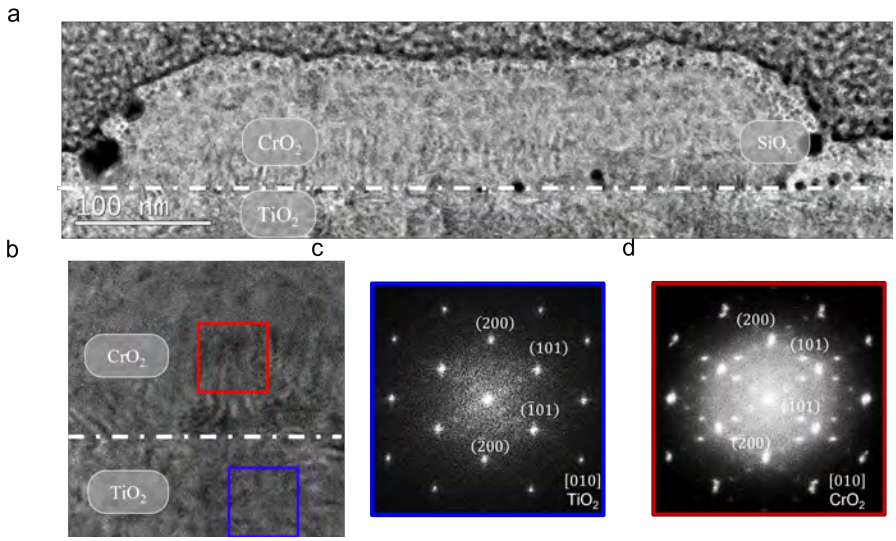

Figure 3.6: TEM inspection of a cross-section from the CrO_2 nanowire along the hard axis . (a) A low resolution TEM image of the TiO_2 substrate at the bottom and the partially grown CrO_2 nanowire in between the SiO_x mask. (b) A high resolution TEM image of the interface between the TiO_2 substrate and the CrO_2 nanowire (c) The indexed FFT of the blue box in (b). The FFT shows the hexagonal diffraction pattern of the TiO_2 substrate with a [010] zone axis. (d) The indexed FFT of the red box in (b). The CrO_2 FFT has the same hexagonal diffraction pattern as in (c) but has extra diffraction spots that are rotated with respect to the main hexagonal diffraction pattern. The complete indexation of all the diffraction spots in (d) is given in the Appendix, sec. 3.8.6.

to rotated, double, and half reflections inside the crystal lattice. This indicates that the CrO_2 nanowire has many crystal domains that are all rotated with respect to each other at specific angles. This Moiré pattern is present in the entire hard wire. This is different from the easy wire, where only small crystal domains along the TiO_2 and CrO_2 interface had a different crystal orientation. A complete indexation of all diffraction spots in Fig. 3.6(d) can be found in the Appendix, sec. 3.8.6.

3.5.2. Magnetotransport

Fig. 3.7(a) shows the longitudinal MR behavior at 10 K for a *hard* wire (the same hard wire as measured in section 3.3), with H_a the magnetic field along the wire axis, meaning $H_a \parallel I$, with I the applied current. Now, the results are different from both the 2 µm etched bars [14, 15] and from other SA grown hard wires of similar width [24]. Both in the etched bars and the SA grown wires, the MR showed a structure of a maximum followed by a bump, due to the several states the magnetic structure went through in the switching process. This includes an intermediate stripe-domain-like

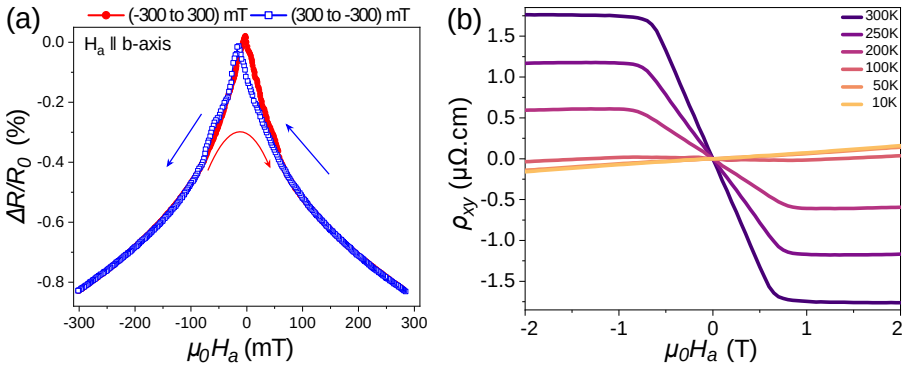

Figure 3.7: Magnetotransport measurements on a hard wire of width 610 nm. (a) In-plane longitudinal MR plot of a hard wire measured at 10 K. The external magnetic field H_a is parallel to the hard wire axis i.e. (H_a || b-axis [010]). The field is swept from −300 mT to 300 mT (filled red circles) and then from 300 mT to −300 mT (open blue squares). The arrows in blue and red show the sweep direction for the respective curves. (b) Hall resistivity as a function of external out-of-plane field for the same hard wire measured at various temperatures between 10 to 300 K. A 100 μA current is applied in both cases.

stable configuration, with the in-plane magnetization perpendicular to the wire (and therefore along the easy axis). Here, we observe a single maximum and only a small amount of hysteresis, indicating that the magnetization along the wire axis is subject to a single domain switching with only minimal additional magnetic disorder. This suggests that the shape anisotropy still plays a significant role in our 610 nm wide hard wire, unlike earlier SA-grown wires where magneto-crystalline anisotropy already dominated the shape anisotropy at a width of 350 nm.

Also the Hall measurements on the hard wire differ when comparing to the previous studies. Fig. 3.7(b) shows ρ_{xy} for different temperatures in a range from 300 K to 10 K. The behavior again follows Eq. (3.1) but the values for $\rho_{xy}(0)$ are almost 50% larger than for the easy wires of similar width. For $\rho_{xy}(0)$ at 300 K, in particular, we find a value of 1.75 $\mu\Omega$cm, compared to 1.1 $\mu\Omega$cm for the easy wire. The significance of this result is that it shows the hard-axis material to be different from the soft-axis material, as actually seen from the HR-TEM results described in sec 3.5.1. For a single type of material, Onsager's principle would say that $\rho_{xy} = -\rho_{yx}$ regardless of crystal orientation, as was indeed found for etched bars [29].

3.6. Wider hard wires

To further investigate the unexpected MR and AHE results obtained for the 610 nm hard wire, we fabricated wider hard wires, with widths of approximately 1.10 µm, 1.67 µm, and 2.26 µm. TEM images from cross-sections of these wires can be found

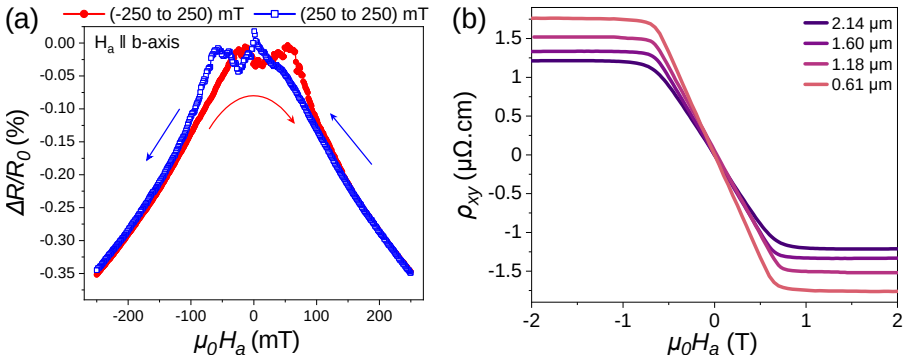

Figure 3.8: Magnetotransport measurements on hard wires of different widths. (a) In-plane longitudinal MR plot of a hard wire of width 1.1 µm measured at 10 K. The applied external magnetic field H_a is parallel to the hard wire axis i.e. (H_a || b-axis [010]). The field is swept from −250 mT to 250 mT (filled red circles) and then from 250 mT to −250 mT (open blue squares). The arrows in blue and red show the sweep direction for the respective curves. (b) Comparison of Hall resistivity as a function of external out-of-plane field for the hard wires of different widths measured at 300 K shows a clear trend of $\rho_{xy}(300)$ decreasing as the width increases.

in the Appendix, sec.3.8.5. Although no significant morphological differences were observed between hard wires of varying widths, including the wire from section 3.5.1, the transport measurements revealed a dependence on the width. Fig. 3.8(a) shows typical MR behavior of the 1.10 µm wire at 10 K. Here, we see the double maximum structure which is similar to the MR behavior observed in previous studies for films and wires.[14, 15, 24] This suggests that at a width of around 1 µm, the point is reached where magnetocrystalline anisotropy dominates shape anisotropy. We observe a similar trend in the Hall data. Fig. 3.8(b) compares the Hall resistivity at 300 K on hard wires of different widths. As the width increases, $\rho_{xy}(0)$ at 300 K decreases and gets closer to the value obtained for the easy wire described in sec 3.4.2. It is likely that for hard wires wider than 2 μm, the behavior of the hard and easy wires becomes comparable, and that we are then essentially in the film regime. This can be understood from a growth point of view, since typical crystallites in films have dimensions of the order of a few μm. A trench of that width will have less confining influence on the growth.

3.7. Conclusion

In summary, we have shown that we can grow high quality CrO_2 nanowires using the Selective Area (SA) growth on a TiO_2 substrate along both the c-axis (easy axis) and the b-axis (hard axis). For the best results, a high degree of control over the etching of the trench is required. Growing hard wires is more challenging due to

higher lattice mismatch between TiO_2 and CrO_2 along the *b*-axis. High-resolution TEM imaging shows that the material has a different morphology on the nanoscale, with the presence of multiple crystal domains that are rotated with respect to each other. The electrical and magnetic properties of the wires generally are in line with the picture coming from TEM.

Our wires are found to be highly conductive, in particular the easy wires, with a room temperature value for ρ_{300} of 120 μΩcm and an RRR of 21. Hard wires are less conducting , as can be expected from the TEM results. The same is true for magnetotransport properties where we find very sharp switching for quite wide easy wires, and different behavior for hard wires. Of special interest is the difference in the AHE for both wire types, which once more reflects the difference in morphology. When trenches become wider than roughly 2 μm, the differences between (easy) *c*-axis wires and (hard) *b* axis wires disappear.

3.8. Appendix

3.8.1. Methods: TEM sample preparation and measurements

The cross-sections of the various nanowires were prepared for TEM inspection using a Focused Ion Beam (FIB) system (The Thermo Scientific™ Helios™ G4 CX DualBeam™ System). The acceleration voltage for the ion beam was set at 30 kV. Before starting the FIB process, a thin layer of gold was sputtered on top of the samples in order to prevent chairing effects on the insulating TiO_2 substrate. During the FIB process the CrO_2 nanowire was protected by a platinum layer, deposited in situ using a MultiChem™ system. Tungsten was used whenever platinum was unavailable. The TEM measurements were carried out using a Thermo Scientific™ Titan 60-300 cubed TEM, operated at 300 kV. The TEM samples were oriented in a zone-axis using a double tilt holder. The HR-TEM images were recorded using a Thermo Scientific™ Ceta-16M CMOS camera.

3.8.2. Crystal structure of CrO_2 and TiO_2

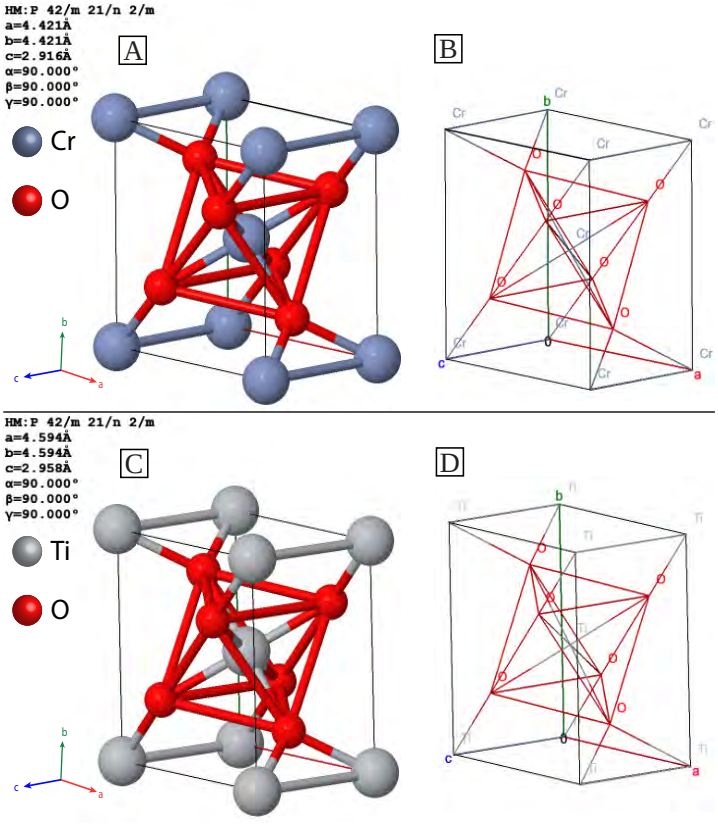

Figure 3.9: The unit cell for CrO_2 (a-b) and TiO_2 (c-d), respectively. Both materials have a rutile structure and are described by a body-centered cubic (bcc) tetragonal unit cell. The lattice parameters of the CrO_2 unit cell are a = b = 4.421 Å and c = 2.916 Å. [33] There are two Cr atoms in the cell, at positions (0,0,0) and $(\frac{1}{2},\frac{1}{2},\frac{1}{2})$. Oxygen atom form octahedra around Cr-atoms and are both side-sharing and corner-sharing. The four oxygen atoms are at [u,u,0] and their symmetric equivalents; where $u = 0.303$. The lattice parameters of the TiO_2 unit cell are a = b = 4.594 Å and $c = 2.958$ Å. [34] The chromium atoms are indicated in purple, the titanium atoms in grey, and the oxygen atoms in red. These models are generated using Eje-Z [35, 36]

3.8.3. Growth morphology and correlation between the width of a nanowire and the direction of growth

CrO_2 crystallites nucleate uniformly at the bottom of the trench on top of TiO_2 surface which merge together to form a continuous surface covering the full width of the trench as shown in Fig. 3.10. The vertical growth then occurs epitaxially. Important to note that we do not get pandeo-epitaxy type of growth with internal voids or dislocations as reported in a previous study [25]. In hindsight, this may have been caused by incomplete etching of the trench bottom. Depending on the direction of growth, the actual width of the wires varies. For the wires along [001] and [010] the width is same as the width of the trench and we do not see any lateral overgrowth on the SiO_2 surface outside the trench. For any other intermediate direction of nanowires, we found lateral overgrowth outside the trench wall, thereby making the actual width of wires larger than the trench width as shown in Fig. 3.11, 3.13 and in Table 3.2. As we increase the time of growth the sideways growth also increases.

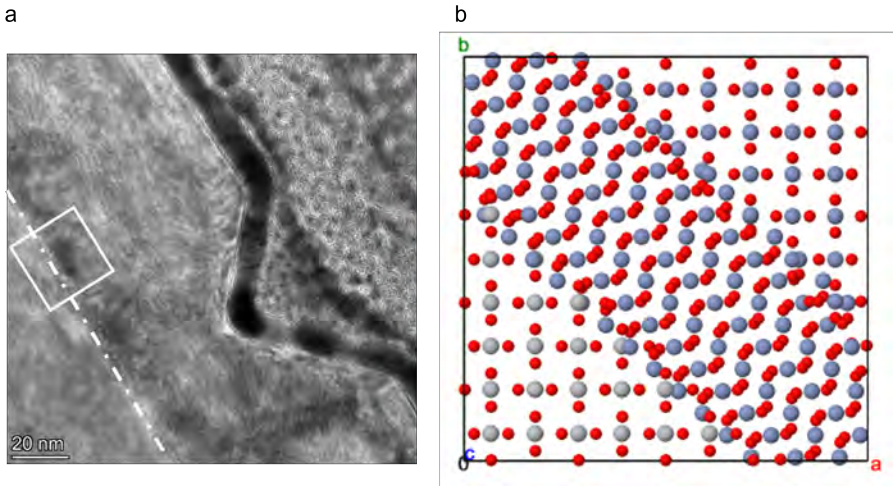

Figure 3.10: (a) TEM image of the same easy wire as depicted in Fig. 3.4(a) in the main text. The CrO_2 wire covers the entire surface of the trench. However, there are areas with different contrast along the interface between the TiO_2 substrate and the CrO_2 wire. A high-magnification TEM image of the area in the white box is displayed in Fig. 3.4 (main text). (b) An atomic model of the interface between the TiO_2 substrate and the CrO_2 wire. The model represents the area in Fig. 3.4(b) (main text), where there are two CrO_2 crystal domains with different orientations.

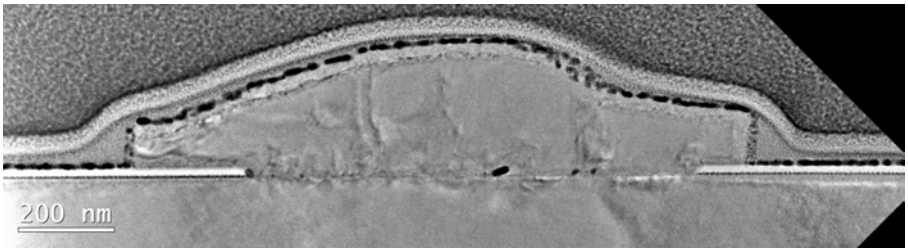

Figure 3.11: Low magnification TEM image of a CrO_2 nanowire where the z-axis is rotated 30° from the easy axis. The nanowire has grown over the SiO_x mask. The nanowire is 1280 nm wide even though the mask is only 925 nm wide.

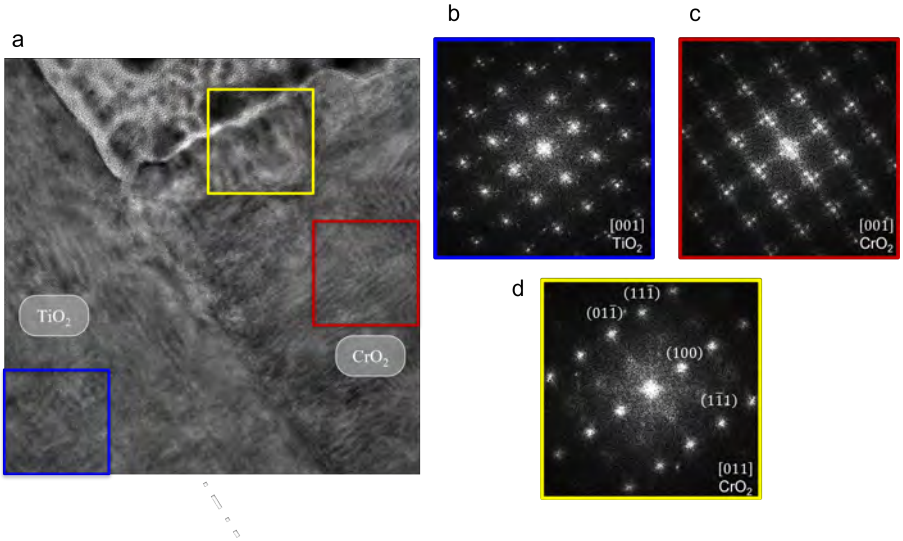

Figure 3.12: High-resolution TEM image of an easy CrO_2 nanowire on top of a TiO_2 substrate at the bottom. The center of the CrO_2 nanowire (red box) has grown epitaxially on the TiO_2 substrate. The FFT of both regions (b-c) shows that both the CrO_2 wire and the TiO_2 substrate (blue box) are oriented in the [001] zone axis. The edge of the CrO_2 nanowire (yellow box) has a different crystal orientation. The FFT of this region (d) is oriented in the [011] zone axis.

3.8.4. The height and width of the CrO_2 nanowire as measured by TEM cross-section

The length and height of the CrO_2 nanowires are measured using TEM images:

Angle (°)	width trench	width wire	max-height wire	min-height wire
0	936	936	177	71
30	925	1280	272	106
45	946	1234	275	175
90	930	982	252	213

Table 3.1: The length and height in nanometers of the nanowires from sample AG_2 for 4 different angles.

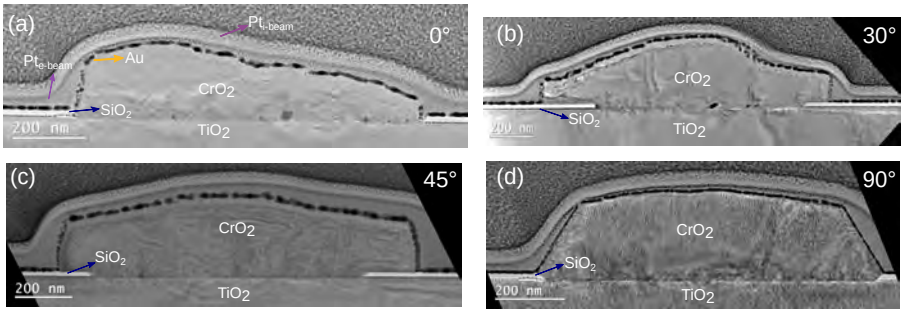

Figure 3.13: TEM image of the sample AG_2 shows the CrO_2 nanowires grown along 4 different angles (0°, 30°, 45°, 90°) with respect to the (100) oriented TiO_2 substrate, where [001] is along the horizontal direction. TiO_2 is at the bottom part, SiO_2 is the narrow white region on both sides of the trench at the interface of TiO_2 and CrO_2 and has been shown with blue arrow while CrO_2 is at the top part. (a) shows the CrO_2 nanowire grown along 0° which is the easy-axis of growth. (b) is at 30° (c) is at 45° and (d) shows the hard-axis CrO_2 nanowire. Both (b) and (c) shows lateral overgrowth of CrO_2 over SiO_2 while (a) and (d) don't show lateral overgrowth.

AG_2 was annealed for 1 hr at 390°C in O_2 at 140 sccm and grown at 260°C for 30 min.

Angle	width trench	width wire	max-height wire	min-height wire
0	514	530	82	41
15	498	528	75	65
30	736	926	77	72
45	498	547	83	80
60	506	559	83	73
90	502	529	104	96

Table 3.2: The length and height in nanometers of the nanowires from sample AJ_2 for 6 different angles.

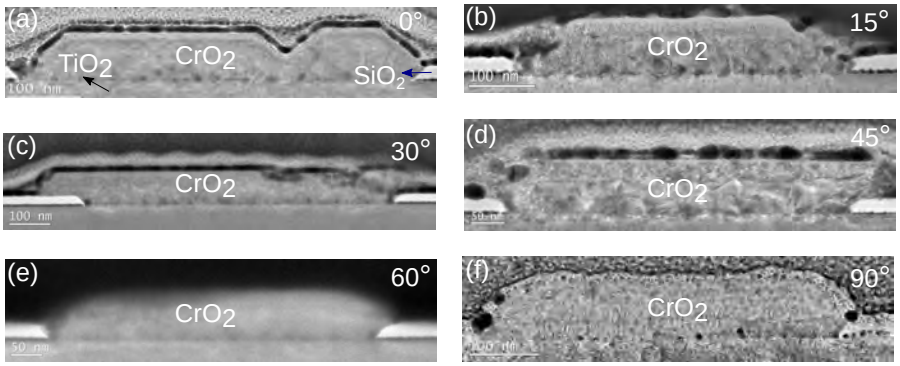

Figure 3.14: TEM image of the sample AJ_2 shows the CrO_2 nanowires grown along 6 different angles (0°, 15°, 30°, 45°, 60°and 90°) w.r.t. TiO_2 substrate where [001] is along the horizontal direction. TiO_2 is at the bottom part, SiO_2 is the narrow white region on both sides of the trench at the interface of TiO_2 and CrO_2 and has been shown with blue arrow while CrO_2 is at the top part. (a) shows the CrO_2 nanowire grown along 0° which is the easy-axis of growth. (b) is at 15° (c) is at 30° (d) is at 45° (e) is at 60° and (f) is at 90°which is the hard-axis of CrO_2 nanowire.

AJ_2 was annealed for 1hr at 390°C in O_2 at 140 sccm and grown at 260°C for 15 min.

3.8.5. TEM images of wider hard nanowires (width $\geq 1\mu m$)

The height and width of the CrO_2 nanowires is measured using TEM images:

AQ_5 was annealed for 1hr at 390°C in O_2 at 140 sccm and grown at 260°C for 35 min.

width trench	width wire	max-height wire	min-height wire
1103	1208	369	332
1672	1810	428	396
2255	2361	472	421

Table 3.3: The height and width in nanometers of the nanowires from sample AQ_5 for three different trench widths.

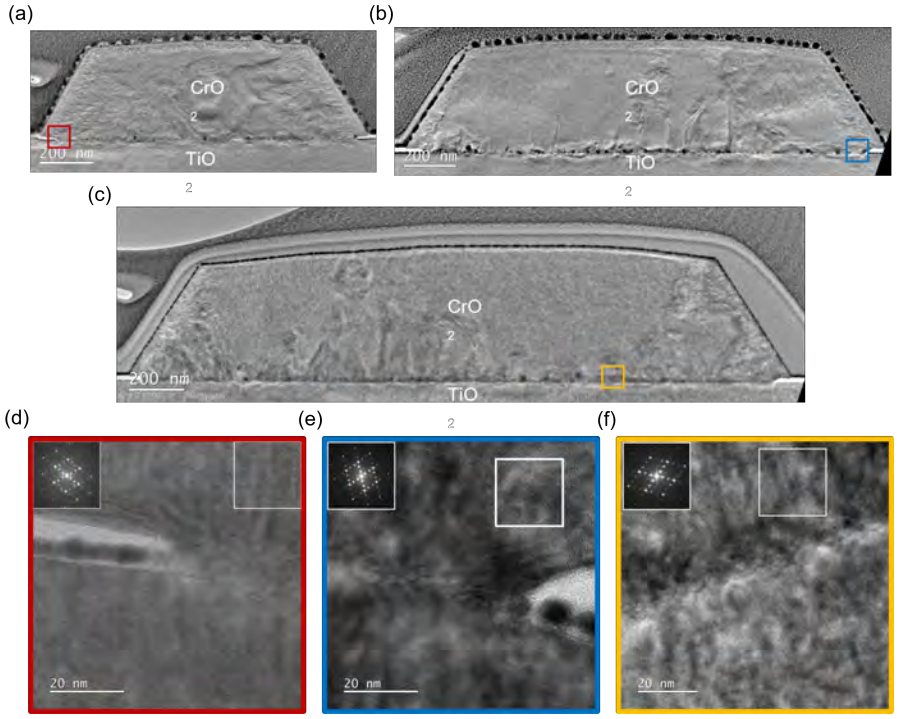

Figure 3.15: TEM images of the sample AQ_5 shows CrO_2 nanowires oriented along the hard axis (90° w.r.t. the [001] TiO_2 substrate). In the first three images (a-c), the TiO_2 substrate is at the bottom, with the CrO_2 nanowire on top. (a) has a trench width of 1103 nm, (b) has a trench width of 1672nm, and (c) has a trench width of 2255 nm. (d-f) HT-TEM images from the CrO_2 and TiO_2 interface for all three nanowires depicted in a-c. The inset shows the FFT of the areas indicated in white. The same Moiré pattern can be seen for all three nanowires. Indicating no change in the CrO_2morphology for the different nanowire widths.

3.8.6. Indexation of the fast Fourier transform shown in Fig. 3.6(d) in main text

Fig. 3.16 contains a FFT of a hard axis CrO_2 nanowire with a zone-axis of [010]. The FFT contains the six diffraction spots belonging to the (200), (101) and $(\bar{1}01)$ family of planes and their inverse. These diffraction spots in this main grouping are denoted by the red letters (A-F). The rest of the diffraction spots belong to the remaining family of planes, listed in the table 3.4-b and labeled by the numbers (1-8). The numbered diffraction spots with the same color all belong to the diffraction grouping. Each grouping of diffraction spots is rotated and/or magnified with respect to the main diffraction grouping (Red A-F). The rotation and magnification factor for each diffraction grouping are listed in table 3.4-a. A clockwise rotation is denoted by a positive angle and a anti-clockwise rotation is denoted by a negative angle.

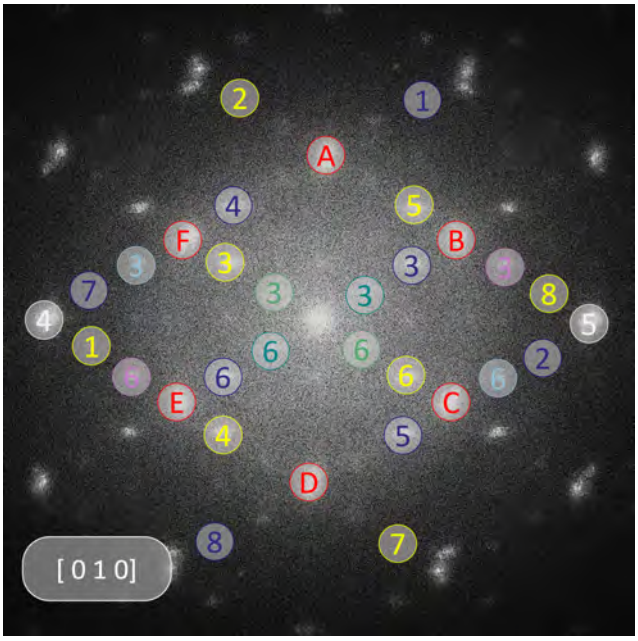

Figure 3.16: Indexation of the FFT of a hard CrO_2 nanowire with a [010] zone-axis

(a)

Grouping	Rotation Angle (°)	Magnification
Red	0	1x
Yellow	-56.7	1x
Dark blue	56.7	1x
Light green	-56.7	2x
Dark green	56.7	2x
Light blue	-74.6	0.5x
Purple	74.6	0.5x
White	0	0.5x

(b)

Letter	(hkl)	Number	(hkl)
A	(200)	1	$(20\bar{1})$
B	(101)	2	(201)
C	$(\bar{1}01)$	3	(100)
D	$(\bar{2}00)$	4	$(00\bar{1})$
E	$(\bar{1}0\bar{1})$	5	(001)
F	$(10\bar{1})$	6	$(\bar{1}00)$
		7	$(\bar{2}0\bar{1})$
		8	$(\bar{2}01)$

Table 3.4: Reference tables for the diffraction indexation of the FFT in Fig. 3.16. (a) Table with the relative rotation and magnification of a diffraction grouping compared to the main diffraction grouping, denoted with the red letters (A-F). (b) Table with the indexation of the family of planes. The main diffraction spots are detonated with the red letters (A-F). The secondary diffraction spots are denoted with by the numbers (1-8).

References

[1] Soulen, R. J. et al. Measuring the Spin Polarization of a Metal with a Superconducting Point Contact. Science **282**, 85–88 (1998).

[2] Zhu, Z. H. et al. Anomalous antiferromagnetism in metallic RuO_2 determined by resonant x-ray scattering. Physical Review Letters **122**, 017202 (2019).

[3] Šmejkal, L., González-Hernández, R., Jungwirth, T. & Sinova, J. Crystal time-reversal symmetry breaking and spontaneous Hall Effect in collinear antiferromagnets. Science Advances **6**, eaaz8809 (2020).

[4] Fujiwara, K. et al. $5d$ iridium oxide as a material for spin-current detection. Nature Communications **4**, 2893 (2013).

[5] Zhang, Z. et al. The high magnetoresistance performance of epitaxial half-metallic CrO_2-based magnetic junctions. Phys. Chem. Chem. Phys. **25**, 1848 (2023).

[6] Qian, L. J., Zhou, S., Wanga, K. & Xiao, G. Resistance of single domain walls in half-metallic CrO_2 epitaxial nanostructures. Nanoscale **13**, 20034 (2021).

[7] Zhang, Z. et al. Ultralow Gilbert damping in CrO_2 epitaxial films. Physical Review B **102**, 14454 (2020).

[8] Qian, L. J., Chen, W., & Xiao, G. Spin curvature induced resistivity in epitaxial half-metallic CrO_2 thin films. Nanoscale **12**, 3958 (2020).

[9] Coey, J. M. D. & Venkatesan, M. Half-metallic ferromagnetism: Example of CrO_2 (invited). Journal of Applied Physics **91**, 8345 (2002).

[10] Kämper, K. P., Schmitt, W., Güntherodt, G., Gambino, R. J. & Ruf, R. CrO_2 - a New Half-Metallic Ferromagnet ? Physical Review Letters **59**, 2788 (1987).

[11] Li, X. W., Gupta, A., McGuire, T. R., Duncombe, P. R. & Xiao, G. Magnetoresistance and Hall Effect of chromium dioxide epitaxial thin films. Journal of Applied Physics **85**, 5585–5587 (1999).

[12] Gupta, A., Li, X. W. & Xiao, G. Magnetic and transport properties of epitaxial and polycrystalline chromium dioxide thin films (invited). Journal of Applied Physics **87**, 6073–6078 (2000).

[13] Miao, G., Xiao, G. & Gupta, A. Variations in the magnetic anisotropy properties of epitaxial CrO_2 films as a function of thickness. Physical Review B **71**, 094418 (2005).

[14] König, C. et al. Micromagnetism and magnetotransport properties of micron-sized epitaxial CrO_2(100) wires. Physical Review B **75** (2007).

[15] Anwar, M. S. & Aarts, J. Anomalous transport in half-metallic ferromagnetic CrO_2. Physical Review B **88**, 085123 (2013).

[16] Anwar, M. S. & Aarts, J. Inducing supercurrents in thin films of ferromagnetic CrO_2. Superconducting Science and Technology **24**, 024016 (2011).

[17] Keizer, R. S. et al. A spin triplet supercurrent through the half-metallic ferromagnet CrO_2. Nature **439**, 825 (2006).

[18] Gönnenwein, S. T. B. et al. Planar Hall Effect and magnetic anisotropy in epitaxially strained chromium dioxide thin films. Applied Physics Letters **90**, 142509 (2007).

[19] Miao, G., Xiao, G. & Gupta, A. Influence of substrate treatment on the growth morphology and magnetic anisotropy of epitaxial CrO2 films. Physica Status Solidi (a) **203**, 1513 (2006).

[20] Gupta, A., Li, X. W., Guha, S. & Xiao, G. Selective-area and lateral overgrowth of chromium dioxide (CrO_2) films by chemical vapor deposition. Applied Physics Letters **75**, 2996–2998 (1999).

[21] Zou, X. & Xiao, G. Magnetic domain configurations of epitaxial chromium dioxide (CrO_2) nanostructures. Applied Physics Letters **91**, 113512 (2007).

[22] Zou, X. & Xiao, G. Half-metallic chromium dioxide (CrO_2) nanostructures and field-dependent magnetic domain evolution. Journal of Applied Physics **103**, 07D710 (2008).

[23] Zou, X., Xiao, G., Huang, S., Chen, T. & Chien, C.-L. Magnetotransport properties of polycrystalline and epitaxial chromium dioxide nanowires. Journal of Applied Physics **103**, 07D710 (2008).

[24] Zou, X. & Xiao, G. Electronic transport and magnetoresistance in polycrystalline and epitaxial CrO_2 nanowires. Physical Review B **77**, 054417 (2008).

[25] Singh, A., Jansen, C., Lahabi, K. & Aarts, J. High-Quality CrO_2 Nanowires for Dissipation-less Spintronics. Physical Review X **6**, 041012 (2016).

[26] Chen, W., Qian, L. & Xiao, G. Resistance of domain-wall states in half-metallic CrO_2. Physical Review B **98**, 174402 (2018).

[27] See Supplemental Material at http://link.aps.org/supplemental/xxx for additional details on the growth morphology of the nanowires as indicated in the main text.

[28] Ye, J. et al. Berry phase theory of the Anomalous Hall Effect: Application to Colossal Magnetoresistance manganites. Physical Review Letters **83**, 3737 (1999).

[29] Yanagihara, H. & Salamon, M. B. Skyrmion strings and the Anomalous Hall Effect in CrO_2. Physical Review Letters **89**, 187201 (2002).

[30] Branford, W. R. et al. Coexistence of universal and topological Anomalous Hall Effects in metal CrO_2 thin films in the dirty limit. Physical Review Letters **102**, 227201 (2009).

[31] Anwar, M. S., Czeschka, F., Hesselberth, M., Porcu, M. & Aarts, J. Long-range supercurrents through half-metallic ferromagnetic CrO_2. Physical Review B **82**, 100501R (2010).

[32] Sousa, P. M. et al. Influence of growth temperature and carrier flux on the structure and transport properties of highly oriented CrO_2 on $Al_2O_3(0001)$. Chemical vapor Deposition **13**, 537 (2007).

[33] CrO_2 crystal structure: Datasheet from "Pauling File Multinaries Edition – 2012" in Springer Materials (https://materials.springer.com/isp/crystallographic/docs/sd_-0534987) (2012). URL `https://materials.springer.com/isp/crystallographic/docs/sd_0534987`. Copyright 2016 Springer-Verlag Berlin Heidelberg & Material Phases Data System (MPDS), Switzerland & National Institute for Materials Science (NIMS), Japan.

[34] TiO_2 crystal structure: Datasheet from "Pauling File Multinaries Edition – 2012" in Springer Materials (https://materials.springer.com/isp/crystallographic/docs/sd_-0304559) (2012). URL `https://materials.springer.com/isp/crystallographic/docs/sd_0304559`. Copyright 2016 Springer-Verlag Berlin Heidelberg & Material Phases Data System (MPDS), Switzerland & National Institute for Materials Science (NIMS), Japan.

[35] Bernal, S. et al. High-resolution electron microscopy investigation of metal–support interactions in Rh/TiO_2. J. Chem. Soc., Faraday Trans. **92**, 2799–2809 (1996). URL `http://dx.doi.org/10.1039/FT9969202799`.

[36] Pérez-Omil, J. Tem-uca user global server (2018). URL `http://www.temserver.uca.es`. University of Cádiz.